Proceedings World Geothermal Congress 2020+1
Reykjavik, Iceland, April - October 2021

Design and Analysis of Two-Phase Geothermal Energy Turbine in Project Combi-Gen

Sham Rane[1*], Li He[1], Zhibin Yu[2] and Guopeng Yu[2]

[1]Department of Engineering Science, Southwell Laboratory, University of Oxford, Oxford, OX2 0ES, UK.

[2]School of Engineering, James Watt Building (South), University of Glasgow, Glasgow, G12 8QQ, UK

*email: sham.rane@eng.ox.ac.uk

Keywords: Geothermal Energy, Two-Phase Turbine, Total Flow System, Computational Fluid Dynamics, Eulerian-Eulerian Multiphase, Two-phase Turbine Test Rig.

ABSTRACT

The Combi-Gen consortium has been established to design and develop geothermally sourced combined power and freshwater generation technology in eastern Africa. The proposed thermal plant consists of a total flow two-phase turbine and a passive thermal chimney for condenser operation. In a total flow system, the high pressure and temperature geothermal fluid is directly passed through the power turbine. During the expansion process, there is flash boiling, generating steam which has very high specific volume and an abrupt increase in fluid volume makes the turbine passage difficult to be designed. Due to this reason, all traditional geothermal turbines have been operated as flash steam turbine using nozzles or binary cycle plants using heat exchange with clean working cycle fluids resulting into high system losses. In this paper, a computational fluid dynamic model of the two-phase turbine has been presented. Flash boiling has been incorporated through the thermal phase change approach that is based on local thermal non-equilibrium with homogeneous nucleation in order to estimate the rate of mass transfer between the liquid and vapour phases. Using this CFD model, a Fabris turbine design has been analysed to reduce inlet and exit losses and optimize the specific work output. A 1.0 KW turbine operating at 500 – 800 kPa well head pressure and exhausting to atmospheric pressure has been designed with estimated fresh water recovery of 8% and isentropic power generation efficiency of 6.8%. The turbine has been analysed at three conditions of 20º, 10º subcooled and saturated inlet water temperature. The feed water flow rate was lower at higher inlet temperatures thus improving the specific power of the turbine. However, the improvement in isentropic efficiency was not observed as the available enthalpy at inlet is higher for higher feed water temperatures. Turbine power increased as the feed water temperature was increased. At saturated inlet condition, the maximum power that could be produced was 2.08 kW at 4623 rpm. Exit vapour quality improved with increase in feed water temperature and was found to be in the range 0.085 to 0.11. Full-scale Combi-Gen thermal plants will be installed at suitable wells identified in the eastern regions of Africa where active geothermal wells have been sourced by the partnering organisations.

1. INTRODUCTION

Geothermal hot water is a natural source of high temperature and high pressure fluid. Across the globe, techniques and systems to utilize the potential of geothermal wells are being explored. Output electrical energy or mechanical energy is found to be the preferred means of extracting the thermal energy contained in the geothermal well. At sites such as in Iceland, Africa, America, Italy, Australia several projects are under-way. As a part of the Combi-Gen consortium established in 2017, a thermodynamic system for combined power generation and pure water co-generation has been aimed (*Yu*, 2019). This is due to the demands at sites in East Africa, Ethiopia, and Kenya where geothermal wells can be tapped but the local population is in greater demand for drinkable water, as is the shortage of clean power supply. In the context of mechanical power generation from geothermal fluids, an impulse type steam turbine has been a classical approach. The systems employing binary fluids such as organic fluids have found use in low temperature heat sources due to their flammability at higher temperature. In high temperature source wells, the geothermal water is initially flashed and steam so produce is used to drive the turbine. The total-flow concept, which is shown in Figure 1, directly uses the geothermal water as the turbines working fluid and is the most efficient means of energy conversion. However the system suffers from the backdrop of heavy mechanical erosion of the turbine, nozzle and mineral deposition which leads to in-operation of the equipment in due course.

Austin et al. (1973) have presented the Total flow concept for power recovery for application to the Salton Sea geothermal bed. Geothermal water was allowed to expand from a pressure of 151.685 bar at a temperature of 300 °C to 27.579 bar. Thermal energy was converted to kinetic head by expansion through a converging-diverging nozzle. The jet was then used to drive an impulse turbine. Similar concepts can be found in literature that have used multi-phase nozzles. *Elliot* (1982) has reported tests with water and nitrogen mixtures and with single stage and two stage impulse turbines. A special two-phase nozzle with mixer housing and liquid injection tube was designed to vary the mass ratio of liquid to vapour in the two-phase flow investigation. *Abuaf et al.* (1981) conducted an extensive experimental study on two-phase flow in a converging-diverging nozzle. The test data is available at various operating conditions in the form of pressure measurements across several points along the length of the nozzle. Vapour void fraction measurements have also been documented in this report and the data is highly suitable for conducting a computational model validation. A closed loop system to heat, pressurize and control the water flow and condenser pressure and temperature was used in these experiments. More recently, *Date et al.* (2015a, 2015b) have presented experimental results of a curved nozzle total flow reaction turbine for low temperature feed water application and reported a maximum isentropic efficiency of 25%. Two-phase CFD modelling of the BNL nozzle (*Abuaf et al.*, 1981) has been analysed using the Thermal Phase-Change model in *Liao and Lucas* (2015). They have extensively reported the influence of various modelling parameters, closure models and grid dependency. Results have been reported in the form of pressure drop along the nozzle, vapour void fraction along the nozzle and across several transverse planes and compared with the BNL test data. A good match of the overall mass flow rate through the nozzle, pressure drop and average void fraction at the exit were reported. In their simulations, the liquid side heat transfer coefficient was formulated based on Jacob number and Peclet number while the vapour side heat transfer was formulated using two resistance approach across a spherical

bubble surface whose diameter was specified using Bubble number density. Grid refinement reported in this study showed an optimum node count of 744,800 for the nozzle geometry and the numerical solver used was ANSYS CFX in steady state. Water data for both liquid and vapour phase was specified using the IAPWS-IF97 equations. Several test points and operating conditions were validated in this study. Particularly, discrepancies in the distribution of radial void fraction were reported. This literature provides a CFD modelling foundation for the approach used in the current study. In order to evaluate the radial void fraction discrepancies in detail, *Janet et al.* (2015) studied the influence of nucleation model using a Bubble number transport equation instead of directly fixing a Bubble number density as was done by *Liao and Lucas* (2015). Small improvements in prediction were observed but were not satisfactorily validated with the BNL measurements. In addition to Bubble number transport formulation, *Janet et al.* (2015) also considered the bubble breakup and coalescence in their model.

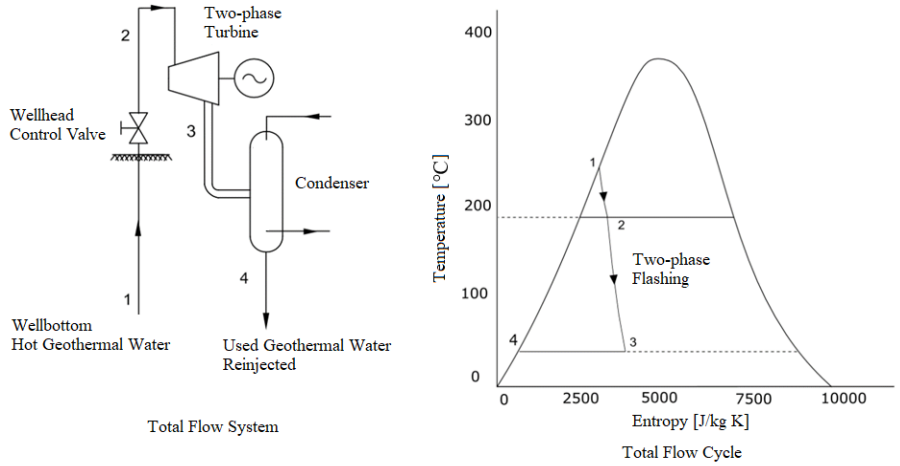

Figure 1: Total Flow System with Two-Phase turbine and Total Flow Cycle (*Smith*, 1993).

In this paper, the modelling of two-phase flow using ANSYS CFX solver has been presented to analyse the design of a base test turbine. An Eulerian-Eulerian multiphase model has been used in the numerical solver. Two-phase heat, mass and momentum transfer has been modelled using the Thermal Phase-Change model. Satisfactory results of flash boiling of liquid water to vapour were achieved by the model and turbine performance data was compared with measurements reported in literature (*Date et al.*, 2015). This two-phase model was then used to redesign the turbine such that flow losses identified in the base turbine could be eliminated. Further the operating condition of Combi-Gen project is not the same as the base turbine; especially the turbine exit pressure. Hence, in other to achieve power output at high turbine exit pressure, the required feed water pressure was evaluated along with the performance estimate at varying feed water temperature of 150°C, 160°C and 170°C. These correspond to 20º, 10º sub-cooled and saturated condition of the feed water at 800 kPa pressure, respectively. The curved nozzle channel re-design is based on evaluation of specific torque variation, pressure distribution and a higher specific power output.

2. TWO-PHASE CFD MODEL

In the Eulerian-Eulerian approach of multiphase CFD modelling, the primary and secondary phases are treated as interpenetrating continua. Phasic volume fraction α_q represents the volume of a computational cell occupied by q^{th} phase and the conservation transport equations of mass, momentum, energy and other scalars are satisfied by each phase individually.

Conservation of mass:

Continuity equation for the q^{th} phase is

$$\frac{\partial}{\partial t}\alpha_q\rho_q + \nabla\cdot\left(\alpha_q\rho_q\,\vec{V}_q\right) = \sum_{p=1}^{n}\left(\dot{m}_{pq} - \dot{m}_{qp}\right) + S_q \tag{1}$$

Here, $\vec{V}_q$ is the velocity of phase q and has three Cartesian components. $\dot{m}_{pq}$ is the mass transfer term from p^{th} phase to q^{th} phase. $\dot{m}_{qp}$ is the mass transfer term from q^{th} phase to p^{th} phase. S_q is any additional mass source for the phase q.

Conservation of momentum:

Momentum conservation for phase q is

$$\frac{\partial}{\partial t}\left(\alpha_q\rho_q\,\vec{V}_q\right) + \nabla.\left(\alpha_q\rho_q\,\vec{V}_q\,\vec{V}_q\right) = -\alpha_q\nabla p + \nabla\cdot\bar{\bar{\tau}}_q + \alpha_q\rho_q\vec{g} + \sum_{p=1}^{n}\left(\vec{R}_{pq} + \dot{m}_{pq}\vec{V}_{pq} - \dot{m}_{qp}\vec{V}_{qp}\right) + \sum\vec{F}_q \tag{2}$$

$$\bar{\bar{\tau}}_q = \alpha_q\mu_q\left(\nabla\vec{V}_q + \nabla\vec{V}_q^{\,T}\right) + \alpha_q\left(\lambda_q - \frac{2}{3}\mu_q\right)\nabla\cdot\vec{V}_q\,\bar{\bar{I}}$$

Where, $\bar{\bar{\tau}}_q$ is the q^{th} phase stress-strain tensor with components that are function of shear and bulk viscosity. p is the pressure shared by all phases, μ_q and λ_q are the shear and bulk viscosity of phase q. $\sum \vec{F}_q$ represents all external body forces such as lift, virtual mass, turbulent dispersion etc. $\vec{R}_{pq}$ is the interaction force between phases such as drag and interphase momentum exchange. $\vec{V}_{pq}$ and $\vec{V}_{qp}$ are the interphase velocities.

Conservation of energy:

Enthalpy conservation equation for phase q is

$$\frac{\partial}{\partial t}\left(\alpha_q \rho_q\, h_q\right) + \nabla \cdot \left(\alpha_q \rho_q\, h_q\, \vec{V}_q\right) = \alpha_q \frac{dp_q}{dt} + \bar{\bar{\tau}}_q : \nabla \vec{V}_q - \nabla \vec{q}_q + S_q + \sum_{p=1}^{n}\left(Q_{pq} + \dot{m}_{pq} h_{pq} - \dot{m}_{qp} h_{qp}\right) \tag{3}$$

$$Q_{pq} = \text{ﬕ}_{pq} A_i \left(T_p - T_q\right) \text{ and } \text{ﬕ}_{pq} = \frac{k_q Nu_p}{d_p}$$

Here, h_q is the specific enthalpy of phase q. $\vec{q}_q$ is heat flux, S_q is enthalpy source, Q_{pq} is the intensity of heat exchange between phases p and q. h_{pq} is the interphase enthalpy i.e. vapour enthalpy in case of evaporation. ﬕ$_{pq}$ is the heat transfer coefficient at the phasic interface, k_q is the thermal conductivity of phase q , Nu_p is Nusselt number and d_p is the vapour bubble diameter of phase p.

2.1 Thermal Phase-Change Model

Within the Eulerian multiphase framework, the Thermal Phase-Change model defines the mass transfer rates entirely based on the interphase heat transfer and overall heat balance at the phasic interface. At the water-liquid and water-vapour interface heat balance gives

$$Q_w + Q_v = 0$$

From the interface to water-liquid phase,

$$Q_w = \text{ﬕ}_w A_i (T_{sat} - T_w) - \dot{m}_{wv} \cdot H_{ws}$$

From the interface to water-vapour phase,

$$Q_v = \text{ﬕ}_v A_i (T_{sat} - T_v) + \dot{m}_{wv} \cdot H_{vs} \tag{4}$$

Sub-script s is selected depending on evaporation or condensation

$$\text{ﬕ}_w A_i (T_{sat} - T_w) - \dot{m}_{wv} \cdot H_{ws} + \text{ﬕ}_v A_i (T_{sat} - T_v) + \dot{m}_{wv} \cdot H_{vs} = 0$$

$$\dot{m}_{wv} = \frac{\text{ﬕ}_w A_i (T_{sat} - T_w) + \text{ﬕ}_v A_i (T_{sat} - T_v)}{H_{vs} - H_{ws}}$$

The interphase mass transfer in equations (1, 2 and 3) are obtained from equation (4). Equation (5) and (6) are used to select the enthalpy for source in equation (3).

If $\dot{m}_{wv} > 0$ (Boiling),

$$H_{ws} = H_w(T_w) \tag{5}$$
$$H_{vs} = H_v(T_{sat})$$

If $\dot{m}_{wv} < 0$ (Condensation),

$$H_{ws} = H_w(T_{sat}) \tag{6}$$
$$H_{vs} = H_v(T_v)$$
$$L = H_v(T_{sat}) - H_w(T_{sat}) \tag{7}$$

As seen from equation (4), heat transfer coefficients ﬕ$_w$, ﬕ$_v$ and interfacial area A_i are required to be determined in the Thermal Phase-Change model. These inputs are prescribed by specifying the interface Nusselt numbers and then calibrating it such that vapour dryness fraction is within a range of an isentropic process (expansion in the nozzle).

3. TWO-PHASE TURBINE DESIGN

For radial outflow type (*House*,1978) of two-phase turbines, *Fabris* (1993) identified that a high inlet pressure to the two-phase nozzle entry, resulting from the centrifugal acceleration of the liquid flowing radially outwards, thereby sub-cooling it and delaying the flashing was a deficiency of the configuration. As an improvement, he proposed a nozzle configuration as shown in Figure 2a to

minimize the lateral forces on the accelerating and expanding fluid and to maximize the length of the nozzle in which expansion took place. The pressure drop along the length of the diverging section of the curved nozzle is assumed to be linear and the change in relative velocity of the fluid along the length of the nozzle is also assumed to be linear. Two-phases tend to separate within the curved nozzle due to the large lateral acceleration and by designing the nozzle curvature using these linear assumptions, the lateral components of Coriolis acceleration, centripetal acceleration relative to motion and centripetal acceleration with respect to turbine axis can be balanced. Efficiencies of up to 50% have been reported from tests carried out on a turbine with this configuration (*Fabris*, 2005). It was claimed that efficiency could be further improved by additional stages (*Smith*, 1993).

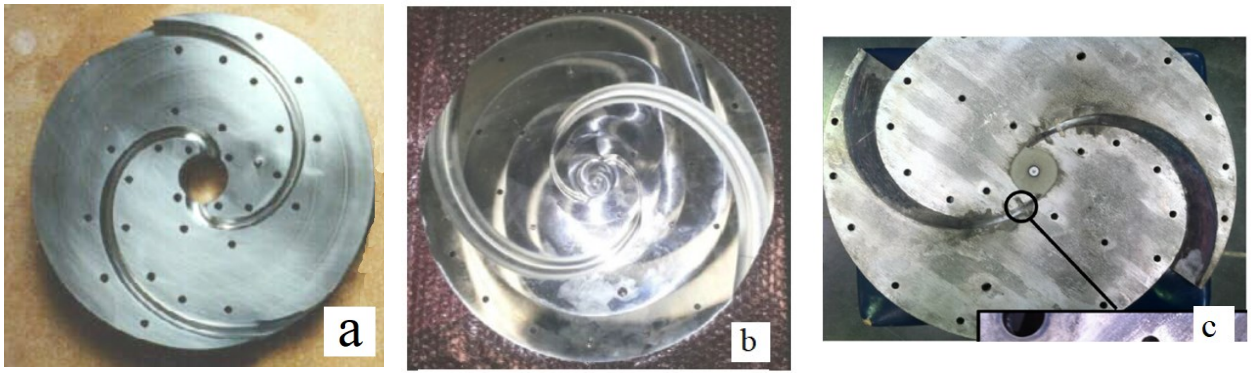

Figure 2: Two-Phase turbines, a – Fabris Design (*Fabris*, 1993), b – RMIT Design (*Date et al.*, 2015a), c – RMIT SDRT Design (*Date et al.*, 2015b).

Date et al. (2015a) have presented experimental performance of a curved nozzle two-phase reaction turbine. Their curved nozzle design was also based on the curvature calculation procedure described in *Fabris* (1993). A variable circular cross section as shown in Figure 2b was used for the channel. They have reported test results from two operating feed water temperatures, for first test the average feed water temperature was maintained around 97°C under local atmospheric pressure, and for the second test the average feed water temperature was maintained around 117°C. For both the tests, the initial condenser pressure was maintained around 6 kPa. The maximum power output of the turbine was estimated to be around 1330 W with an isentropic efficiency of around 25%. The turbine operation was not continuous due to limits of the condenser to handle higher mass flow rates, which eventually raised the 6 kPa back pressure with time. The test lasted for approximately 150 seconds of acceleration and further 100 seconds of deceleration of the turbine. The CFD modelling of this test turbine has been presented in *Rane and He* (2019).

Another form of a two-phase turbine was investigated by *Date et al.* (2015b), as shown in Figure 2c. This 412mm diameter split disk reaction turbine (SDRT) was designed for a maximum speed of 10000rpm. Two distinguishing features of this rotor are that the channel curvature is formed of circular arcs and the throat is an insert with 2.5mm orifice diameter. Four possible locations for the throat insert were tested. In another variant, a flat head pin was placed downstream of the throat to enhance flashing. The channel cross section is rectangular with an exit size of 33mm x 20mm. Tests have been reported for sub-cooled feed water temperature of 96°C under local atmospheric pressure and the initial condenser pressure was maintained around 6 kPa. Positioning of the throat insert at different radial distances from the center of the turbine influences the centrifugal force induced pressure rise upstream of the throat, thus effecting the flow rate through the nozzles. An optimum location was found to be at 34mm from the center. Above and below this distance the isentropic efficiency of the turbine showed a drop. For optimum insert location, the reported isentropic efficiency was 3.1% and 100 W shaft power output at 670 rpm was produced. Addition of a pin downstream of the throat showed a 70% increase in power output with 6% isentropic efficiency.

3.1 Base Turbine Analysis

The base turbine analysed here is shown in Figure 2b – RMIT design. The turbine has two symmetrically positioned curved nozzles. The feed water pressure of 400 kpa and temperature of 117°C is specified at the inlet to the nozzle. The exit of the turbine is open to a flash tank connected to condenser coil which during the start of the experiments is vacuum conditioned to 6 kPa pressure. The available measurements (*Date et al.*, 2015a) on the base turbine are used as boundary conditions for the CFD model at corresponding operating speed. Specification of the base turbine is listed in Table 1.

Table 1: Base turbine specification (Figure 2b – RMIT design)

Geometry		**Performance**	
Parameter	**Specification**	**Parameter**	**Specification**
Disk Diameter	300.0 mm	Inlet	400 kPa, 117 °C
Inlet Diameter	50.0 mm	Exit	6.0 kPa – Condenser
Thickness	44.0 mm	Turbine Power	1.33 kW
Throat area	2.0 mm Circular	Flow	15.0 lpm
x	0.0 mm	Speed	4600 rpm
y	59.15 mm	Specific Power	89 W/lpm
Channel Length	300.0 mm	Isentropic η	17%
Exit area	25.0 mm Circular	Exit quality x	0.13 kg/kg

The inlet pressure is maintained fixed while the exit pressure is specified as recorded during the measurements. Inlet feed water temperature is specified with liquid volume fraction as 1 and vapour volume fraction as 0. Exit temperature is specified only for backflow definition. The CFD model uses a smaller flash tank domain up to a diameter on 225mm which is defined as pressure outlet boundary condition. CFD computations were performed over a range of operating speed from 1560 to 4623 rpm. Results from the measured data for feed water flow rate, shaft power, exit vapour dryness fraction and isentropic efficiency were used for the validation of the two-phase turbine model.

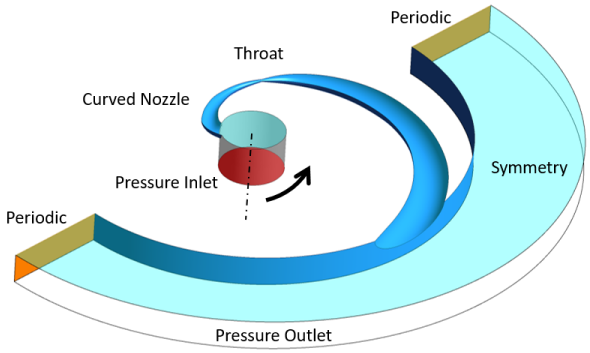

Figure 3: Two-Phase CDF model of base test turbine.

Figure 3 presents the computational domain of the two-phase turbine and the main boundaries. The inlet is specified as pressure acting on an axial cross section of the inlet pipe. Only one of the curved nozzle is included in the CFD model as a 180 degree sector of the turbine has been modelled. Consequently there are periodic boundaries. In order to reduce the grid size further, a symmetry plane is defined at the mid-plane of the turbine. Due to this condition, gravity body force acting along the turbine rotational axis has been excluded from the two-phase model. A moving reference frame is used to apply angular velocity to the turbine.

3.1.1 Channel pressure and vapour distribution

The distribution of pressure on the nozzle surface is presented in Figure 4. From inlet pressure of 400 kPa there is rise in the channel pressure up to 671.8 kPa to the throat of the channel. Even though this is a converging section of the nozzle, the pressure rises due to centrifugal force acting on the fluid. On the downstream of the throat a severe drop in local pressure is observed to about 45 kPa. Only a small difference in pressure is observed between the leading and trailing surface of the nozzle thus indicating a low torque from the radial pressure gradient. Similarly, an evolution of pressure along the axis of the curved nozzle in the turbine mid-plane has been plotted in Figure 5. From inlet to the nozzle throat a steady increase in the fluid pressure is observed. The peak pressure upstream of the nozzle goes up to 671.8 kPa and then severely drops down close to 45 kPa downstream of the nozzle throat. Using this information, the nozzle section could be redesigned in order to avoid the pressure rise which could improve the specific power output of the turbine.

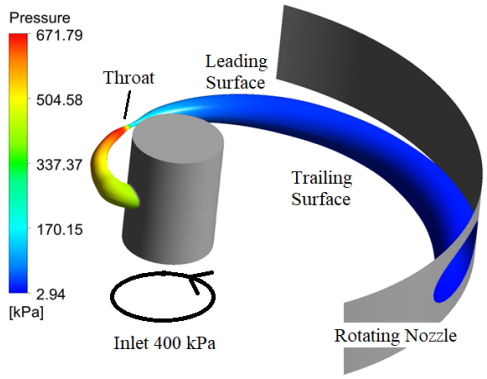

Figure 4: Pressure distribution at 4623rpm on the curved nozzle.

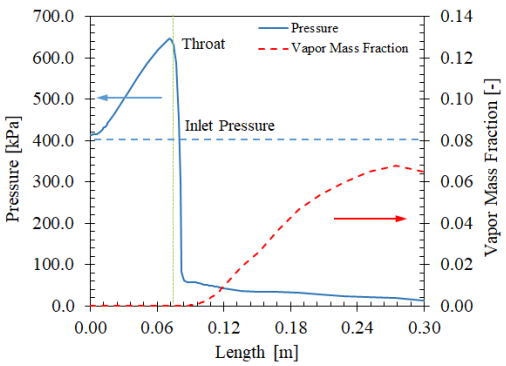

Figure 5: Evolution of pressure and vapour mass fraction along the axis of the nozzle.

Figure 5 also presents the variation of vapour mass fraction along the axis on the nozzle, in the mid-plane. In the converging section, the pressure is high, liquid is subcooled and hence flashing does not occur. Feed water remains in liquid state with no phase transition. Just at the downstream of the throat a severe drop in local pressure is observed to about 45 kPa and this initiates the flash boiling as local saturation temperature is lower than the liquid temperature, according to the governing Thermal Phase-change model. The vapour distribution in this region is observed only close to the nozzle wall and not in the core of the flow. Here, (at 0.06m channel length) the vapour mass fraction is 0%. After the throat (close to 0.08m channel length) the inception of water vapour due to flash boiling is observed. Further downstream due to rotation of the nozzle and the curvature, the flash boiling continues on the trailing surface of the nozzle. At nozzle exit, the mass fraction is about 7% at the centerline.

Figure 6 presents the distribution of vapour dryness fraction in the turbine nozzle at 4623rpm. Flashing initiates just after the throat area and although homogeneous nucleation is set in the CFD model, vapour generation is seen to be high, adjacent to the throat wall.

This effect is due to liquid velocity being relatively high in the core of the flow compared to that at the throat wall, resulting in higher residence time at the throat wall for interphase heat and mass transfer to develop. From the throat region and in the diverging section of the nozzle there is steady increase in vapour fraction. Downstream, the flash development is highly non-uniform and vapour mass fraction is high on the low pressure surface i.e. trailing surface of the nozzle. At the nozzles exit, average dryness fraction is 12%, which is close to the test data of 12.8%. Heavier liquid phase is present on the high pressure i.e. leading surface. This nature of distribution of vapour mass fraction and flashing regime is highly dependent on the turbines rotational speed, though the exit vapour dryness fraction was found to be in the range of 11 – 12% over the entire speed range.

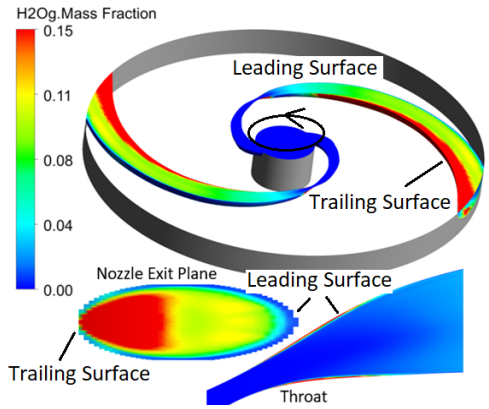

Figure 6: Vapour mass fraction distribution at 4623rpm on the curved nozzle surface.

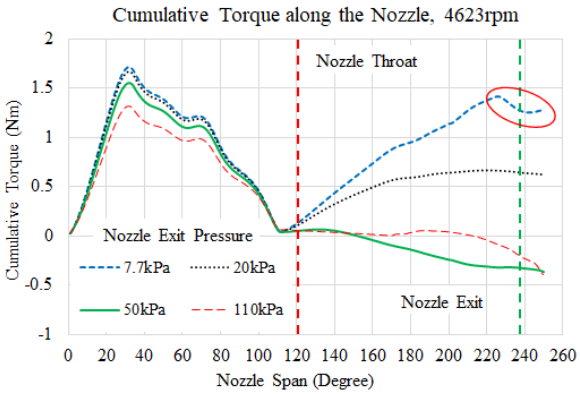

Figure 7: Cumulative torque variation at 4623rpm on the curved nozzle with increasing exit pressure.

3.1.2 Channel torque distribution

A specific torque variation is extracted by scanning the nozzle span with 1° interval. Sum of the specific torque over a certain span of the nozzle is plotted as the cumulative torque variation in Figure 7. Cumulative torque at any specific channel span indicates the net torque output if the nozzle was clipped to that length. From inlet to about 30°, the rotor torque is positive and increasing. After this the nozzle curvature and surface area variation is such that the specific torque becomes negative. This results into a decrease in the net torque, up to the throat section. After the throat section the specific torque again becomes positive and the cumulative torque starts to increase up to the nozzle exit. The base turbine design has a circular disk with tangential exit section and pressure acting on the trailing surface results into a negative specific torque as seen after 220° channel span. This further reduces the cumulative torque and net torque output from this turbine. The nature of torque variation presented in Figure 7 is observed at all speeds of the turbine. Torque analysis provides information on redesign of the inlet and exit of the turbine to eliminate negative specific torque so that net power output and specific power of the turbine can be improved.

3.1.3 Turbine feed water flow and power

The variation of turbine feed water flow with speed and comparison with measurements is presented in Figure 8. It is seen that the CFD model is accurately predicting the nozzle flow and the deviation is in the range of 0.5 – 7.5% over the speed range. The measurement error band was reported as ±7%. This data could be further used to carry out design changes in the turbine to improve the specific power. Deviation is lower at higher speed.

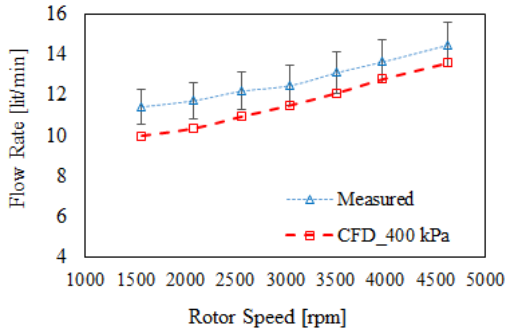

Figure 8: Comparison of feed water flow rate between measurements and CFD model.

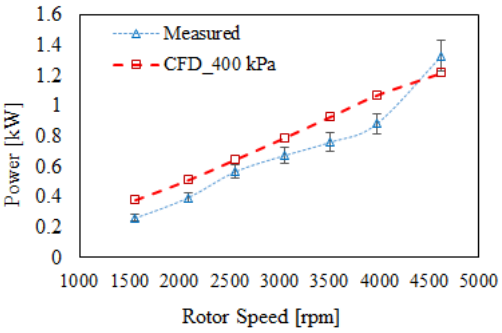

Figure 9: Comparison of turbine power between measurements and CFD model.

The variation of turbine power with speed and comparison with measurements is presented in Figure 9. It is seen that the CFD model is over predicting the nozzle torque and hence the turbine power at operating speeds below 4000 rpm in the range of 30 -55%. At 4623 rpm, the turbine power deviation in the range of 4.5% is observed. The power estimate from CFD model could be used for a comparative study between various nozzle channel designs close to this operating speed. Rotor torque and hence power estimate was found to be dependent on the bubble size, bubble number density and heat transfer parameters prescribed in the CFD model. The vapour dryness fraction at turbine exit was close to an isentropic expansion vapour quality. The isentropic efficiency was 7.5 – 17% for the analysed speed range. Further CFD solution parameters and geometrical parameters are required to be analysed in order to understand the causes for this rotor torque and power deviation.

3.2 Turbine Re-design and Analysis

Analysis of the base turbine provided important features that could be modified in order to improve the power output from the turbine. A reference for this redesign is the cumulative torque variation along the nozzle channel plotted in Figure 7. At an inlet pressure of 400 kPa, a positive turbine torque of 1.29 Nm per nozzle was produced at 4623 rpm when the turbine operated in a vacuum environment i.e. the exit back-pressure of the turbine was very low at 7.7 kPa. While the inlet feed water pressure is held fixed at 400 kPa if the nozzle exit pressure is gradually increased to 20, 50 and 110 kPa then the resulting cumulative torque variation has been plotted in Figure 7. As the nozzle exit pressure increases, the cumulative as well as net torque goes on reducing and finally after about 30 kPa back pressure there is no positive power output from the turbine. In the Combi-Gen thermal system (*Yu*, 2019), the Total Flow Cycle will be employed and the geothermal water exiting from the turbine is required to directly enter a thermal chimney condenser. As such there will be no parasitic pumping losses associated with depressurization of the condensing chamber. To take advantage of natural draft in a thermal chimney, the turbine is required to exit at 110 kPa pressure. This leads to a limitation on the power output that can be produced for a given inlet pressure. In this situation, the feed water pressure has to be increased and the turbine needs to be redesigned. Based on the analysis of the circular cross section channel, other important re-design factor was incorporation of a distinct leading and trailing surface into the channel geometry as radial pressure gradient was very small. One method of introducing distinct leading and trailing surface is by using a square cross-section, which would result into an increase in the specific torque variation along the nozzle. The disadvantage with square cross section is that it increases the flow area by 21.4% for the same dimension as that of the diameter of the corresponding circular cross-section. However, the specific power output increases. The turbine was redesigned with a square channel section and a modified disk with tangential flow exit area, but the nozzle curvature was unchanged from the base turbine design as it had been optimized for balancing of lateral interphase separation forces. Geometry of the redesigned turbine is shown in Figure 10 and the specification is listed in Table 2.

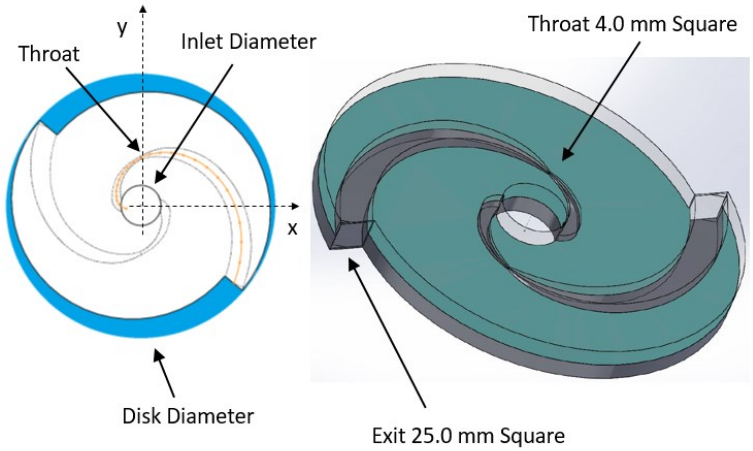

Figure 10: Redesigned turbine with square cross-section, curved nozzle and modified rotor disk with tangential flow exit.

Table 2: Redesigned turbine specification

Geometry		Performance	
Parameter	**Specification**	**Parameter**	**Specification**
Disk Diameter	330.0 mm	Inlet	500 – 800 kPa, 150 – 170 °C
Inlet Diameter	50.0 mm	Exit	110 kPa – Condenser inlet
Thickness	30.0 mm	Turbine Power	1.3 kW
Throat area	4.0 mm Square	Flow	70.0 lpm
x	0.0 mm	Speed	3500 rpm
y	59.15 mm	Specific Power	20 W/lpm
Channel Length	300.0 mm	Isentropic η	6.8%
Exit area	25.0 mm Square	Exit quality x	0.085 kg/kg

In the redesigned turbine's nozzle, the area variation function is maintained same as that of the base turbine channel. The re-designed turbine was analysed with the same numerical setup of the two-phase turbine model. The computational grid density was also maintained equivalent. The Two-phase CFD model of the redesigned turbine is shown in Figure 11. The inlet pressure is maintained fixed at 800 kPa and the exit pressure is specified as 110 kPa. Three inlet feed water temperatures were specified. Inlet liquid volume fraction was set as 1 and vapour volume fraction as 0. Exit temperature is specified as the saturation temperature at 110 kPa, only for backflow definition. Similar to the base turbine model, a smaller flash tank domain of diameter 225mm was used, which is defined as pressure outlet boundary condition. The turbine's performance was estimated at varying feed water temperature of 150°C, 160°C and 170°C. These correspond to 20º, 10º sub-cooled and saturated condition of the feed water at 800 kPa pressure, respectively. Results of feed water flow rate, turbine power and specific power output, exit vapour quality and isentropic efficiency were evaluated over an operating speed range of 1561 to 4623rpm.

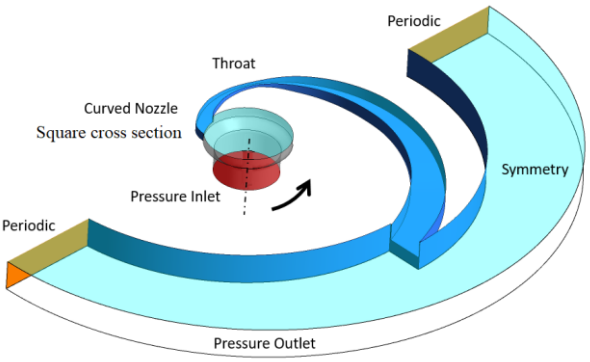

Figure 11: Two-Phase CDF model of redesigned turbine – Square channel, curved nozzle, tangential flow at exit.

3.2.2 Redesigned turbine feed water flow and power

Redesigned turbine was analysed at 800kPa inlet pressure and 110 kPa exit pressure, which is a pressure ratio of 7.3. A comparison of the performance of the turbine at three feed water temperatures and fixed pressure ratio is plotted in Figure 12.

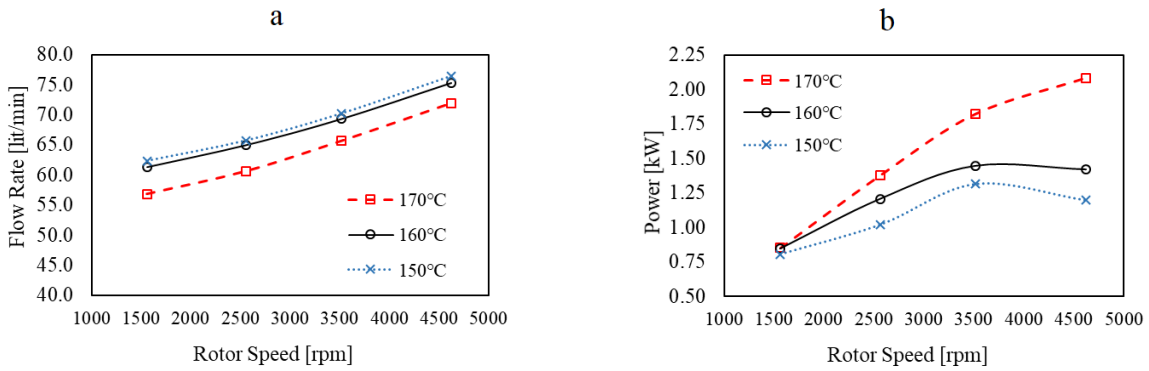

Figure 12: Redesigned turbine at 800kPa inlet pressure. Comparison of, a – feed water flow rate and b – Power output, at three feed water temperatures.

The redesigned turbine has a square channel. Due to this the flow area increased by 21.4% in the cross-section and the water flow increased over the full speed range. In addition to this effect, the throat size in the redesigned turbine is 4.0 mm and the inlet pressure is 800 kPa. Both these factors substantially increased the feed water flow through the redesigned turbine by an average factor of 4.7 as compared to the base turbine. Feed water flow rate, at three feed water temperatures is compared in Figure 12a. Flow through the turbine decreases as the feed water temperature is raised from 150°C to 170°C. This is a positive influence as it contributes towards improvement in specific power output. Average reduction in flow is 9% from 150°C to 170°C.

The square channel in the redesigned turbine has a distinct leading and trailing surface, the negative specific torque at the nozzle exit was eliminated by the modified disk exit, the turbine has a higher flow and 800 kPa inlet pressure. All these factors have contributed to produce a positive power output from the redesigned turbine even though the pressure ratio is just 7.3 and the turbine exit pressure is high, at 110 kPa. The base turbine failed to produce positive power when back pressure increased beyond 30 kPa. Comparison of power output at three feed water temperatures is plotted in Figure 12b. A big influence of feed water temperature is seen on the power output from the turbine. As the feed temperature is raised from 150°C to 170°C, at 3500 rpm, the power increases from 1.3 kW to 1.8 kW. At 160°C power output is intermediate at 1.44 kW. At both 150°C and 160°C the peak of power is observed at 3500 rpm. But at 170°C, the peak power output of 2.08 kW was produced at 4623 rpm.

3.2.2 Redesigned turbine specific power, exit vapour quality and isentropic efficiency

A comparison of derived performance quantities for the redesigned turbine, such as specific power, exit vapour quality and isentropic efficiency are plotted in Figure 13.

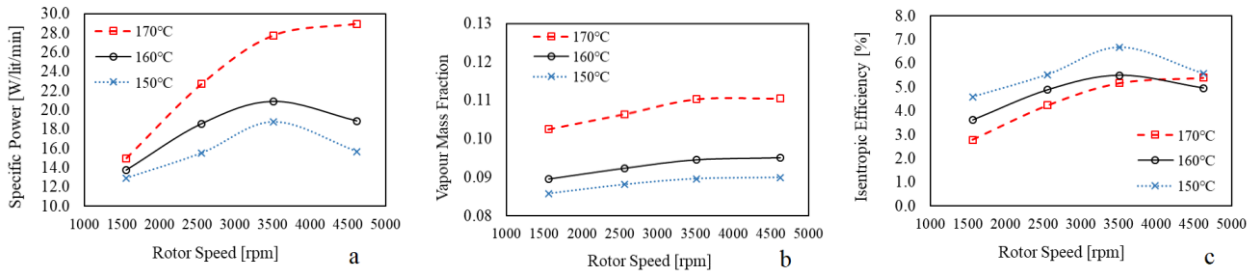

Figure 13: Redesigned turbine at 800kPa inlet pressure. Comparison of, a – specific power, b – exit vapour quality and c – isentropic efficiency, at three feed water temperatures.

The specific power at three feed water temperatures is compared in Figure 13a. As seen, turbine specific power increases with increase in feed water temperature from 150°C to 170°C. This is a combined effect of reduction in flow and increase in the power output with feed water temperature. The vapour quality at the exit of the turbine is compared in Figure 13b. The average vapour quality at turbine exit is 0.088 at 150°C, 0.09 at 160°C and further increases to 0.11 at 170°C thus improving the potential for fresh water recovery from the system. Only a small influence of operating speed was seen on the exit vapour quality, as was also observed in the analysis of the base turbine. The isentropic efficiency of the turbine at three feed water temperatures is compared in Figure 13c. At 150°C, the maximum isentropic efficiency is 6.8% at 3500 rpm. The inlet enthalpy increases with feed water temperature from 632.38 kJ/kg at 150°C, 675.58 kJ/kg at 160°C to 719.09 kJ/kg at 170°C. However, since the exit of the turbine is still at 110 kPa, at all the feed water temperatures, the isentropic enthalpy drop is higher resulting into lower isentropic efficiency at higher feed water temperatures. This indicates that further power could be potentially extracted at higher feed water temperatures by increasing the residence time for liquid phase in the turbine channel. With feed water temperature of 170°C, at 4623 rpm, the isentropic efficiency is 5.4% and the specific power output is the highest at 29 W/lpm. (In comparison, the base turbine operating at a very high pressure ratio ~ 52, the specific power output was 91.8 W/lpm and isentropic efficiency was 17% at 4623 rpm)

4. CONCLUSIONS

The Thermal Phase-Change formulation for modelling of flash boiling flows was applied for the analysis of Two-Phase geothermal turbines. ANSYS CFX solver was used for the study with moving reference frame, periodic and symmetry based model grid size reduction and pressure inlet and outlet boundary conditions. The liquid and vapour fluid properties for water were defined using the IAPWS-IF97 library available within the solver. Interphase heat transfer parameters of Nusselt number correlation and vapour bubble number density were prescribed and the mechanism of interphase mass transfer due to phase change relies on local thermal non-equilibrium with homogeneous nucleation in the model.

- Base turbine flow at various operating speeds was well estimated, within 0.5 – 7.5% deviation from measurements. Nozzle torque and hence turbine power estimate was within 4.5% at 4623rpm. Turbine performance, liquid and vapour distribution and flash boiling boundaries were predicted by the analysis. Nozzle exit vapour dryness fraction was estimated in the range of 0.11 to 0.13.
- Isentropic efficiency of the base turbine varied from 5% at 1561rpm to a maximum of 19% at 4623rpm. CFD model estimated the Isentropic efficiency in the range of 10 to 19% due to the over-estimated power at lower speed.

The turbine was redesigned with a channel having square cross section, a throat diameter of 4mm and the turbine disk was modified to achieve a tangential area at the nozzle exit. The redesign was required in order to eliminate negative specific torque at the nozzle exit as identified in case of circular disks and to obtain near to 1.0 kW power output, when operating at atmospheric back pressure. The redesigned turbine was analysed at 800 kPa feed water pressure and three temperatures of 150°C, 160°C and 170°C that correspond to 20°, 10° sub-cooled and saturated condition of the feed water, respectively.

- The feed water flow rate was lower at higher inlet temperatures thus improving the specific power of the turbine. However, the improvement in isentropic efficiency was not observed as the available enthalpy at inlet is higher for higher feed water temperatures.
- Turbine power increased as the feed water temperature was increased. At saturated inlet condition, the maximum power that could be produced was 2.08 kW at 4623 rpm.
- Exit vapour quality improved with increase in feed water temperature and was found to be in the range 0.085 to 0.11

Alongside the turbine design presented in this paper, a new test facility is being built to test the prototype turbine and measured data will be used for validation and improvement of the turbine and recovery system. This test facility is mainly composed of four sections, including rotating two-phase turbine test section, condenser, evaporator, and thermal-oil heat source. The rotating two-phase turbine test section, based on trilateral flash cycle, will simultaneously generate power and steam, which will then be condensed in the condenser to produce freshwater. The temperature and pressure along the curved turbine channel will be measured with miniatured temperature and pressure sensors. Full scale Combi-Gen thermal plants will be installed at suitable wells identified in the eastern regions of Africa where active geothermal wells have been sourced by the partnering organisations.

ACKNOWLEDGEMENTS

The research is sponsored by UK Engineering and Physical Sciences Research Council (EPSRC GCRF grant EP/P028829/1). Authors would also like to thank Dr Abhijit Date, RMIT, Australia, for providing the reference turbine test data for development and validation of the CFD model.

REFERENCES

Abuaf, N., Wu, B. J. C., Zimmer, G. A., and Saha, P.: A study of Nonequilibrium flashing of water in a converging-diverging nozzle. Brookhaven National Laboratory BNL-NUREG/CR-1864, Volume 1, (1981).

Austin, A. L., Higgins, G. H., and Howard, J. H.: The total flow concept for recovery of energy from geothermal hot brine deposits. Lawrence Livermore Laboratory UCRL-51366, (1973).

Comfort, W. J.: Applicability of the Hero Turbine for Energy Conversion from Low Quality Two-Phase, Inlet Fluids. Proceedings of the Symposium on Polyphase Flow in Turbomachinery, ASME Winter Annual Meeting, (1978).

Date, A., Vahaji, S., Andrews, J., and Akbarzadeh, A.: Experimental performance of a rotating two-phase reaction turbine. *Applied Thermal Engineering* **76**, (2015a), 475-483.

Date, A., Khaghani, A., Andrews, J., and Akbarzadeh, A.: Performance of a rotating two-phase turbine for combined power generation and desalination. *Applied Thermal Engineering* **76**, (2015b), 9-17.

Elliot, D. G.: Theory and Tests of Two-phase Turbines, Jet Propulsion Laboratory 81-105. DOE/ER-10614-1, (1982).

Fabris, G.: Two-phase Reaction Turbine, United States Patent 5,236,349, (1993).

Fabris G.: Two-phase flow turbine for cogeneration, geothermal, solar and other applications. California Energy Commission's Feasibility Analysis and Final EISG Report - CEC-500-2005-079, (2005).

House, P. A.: Performance Tests of the Radial Outflow Reaction Turbine for Geothermal Applications. Lawrence Livermore Laboratory Report UCID-17902, (1978).

Janet, J. P., Liao, Y., and Lucas D.: Heterogeneous nucleation in CFD simulation of flashing flows in converging–diverging nozzles. *International Journal of Multiphase Flow* **74**, (2015), 106–117.

Liao, Y., and Lucas, D.: 3D CFD simulation of flashing flows in a converging-diverging nozzle. *Nuclear Engineering and Design* **292**, (2015), 149–163.

Rane, S., and He, L.: Modelling of flash boiling in two phase geothermal turbine. *Proceedings,* 16th UK Heat Transfer Conference, Nottingham, Paper 005, (2019).

Smith, I. K.: Development of the Trilateral Flash Cycle System, Part 1: Fundamental Considerations. Journal of Power and Energy, Proc IMechE 207-3, 179-194, (1993).

Yu, G., and Yu, Z.: Combined Power and Freshwater Generation Driven by Liquid-Dominated Geothermal Sources. Energies, 12, 1562, (2019).